1990

Differential, Partial Cross Sections for Electron Excitation of the Sodium 3P State

Xianming Han
Butler University, xhan@butler.edu

G. W. Schwinn

A. Gallagher

Differential, partial cross sections for electron excitation of the sodium 3P state

Xianming L. Han,* Gregory W. Schinn,† and Alan Gallagher‡
Joint Institute for Laboratory Astrophysics, National Institute of Standards and Technology and University of Colorado, Boulder, Colorado 80309-0440
(Received 2 January 1990)

Using a powerful laser-based experimental method, the cross section for electron excitation of Na(3S) atoms to the Na(3P) state has been decomposed into partial components with respect to changes in the spin and angular momentum of the atomic electron, and these partial cross sections are further reduced to their differential character with respect to the electron scattering angle. Partial, differential cross sections are reported for electron collision energies from threshold 2.1 to 3.6 eV, and compared to available calculations.

I. INTRODUCTION

Near-threshold electron excitation of atoms plays an important role in many contexts, including fields as diverse as stellar and planetary atmospheres, discharge lamps and lasers, and fusion reactors. Proper understanding of this physical process requires detailed knowledge of the electron-atom collision dynamics and complex calculations, which must include spin-exchange and direct scattering. Here we report a highly detailed experimental study of such an excitation, where the changes in atomic m_L and m_s angular-momentum projections are measured as a function of electron-scattering angle. Changes in m_s are most significant for near-threshold excitation energies, and for low-Z atoms they arise almost exclusively from exchange effects.[1] The present results provide a very detailed test of the collision dynamics in this interesting energy region, as well as providing an overview of the general characteristics of near-threshold excitation.

The concept of the "complete" scattering experiment was articulated by Bederson in 1969.[2] He described how one could measure, in principle, the magnitudes and phases of a finite number of complex scattering amplitudes in order to completely describe any elastic or inelastic electron-atom collision process. In particular, the excitation of the first resonance level (3S-3P) of sodium in the near-threshold energy region can be completely characterized by the measurement of seven parameters (corresponding to four complex amplitudes less an overall phase) at each collision energy and electron scattering angle.

The electron-collisionally-induced Na 3S-3P transition has been very frequently studied, and various experiments have measured partial sets of these parameters, normally for differential electron scattering.[3] In the most definitive experiment to date, the superelastic-scattering, polarized-electron technique of McClelland *et al.*[4] has yielded several combinations of these parameters at several electron-scattering angles for several collision energies between 1.3, and 12.8 eV above threshold.

We report here the results of an experiment which measures four of these seven parameters, and three as a function of electron scattering angle. Specifically, we have measured the dependence of the sodium 3S-3P excitation cross section on changes in m_s and m_L of the atomic electron. Preliminary angle-integrated results for these four partial cross sections have already been published.[5] Improvements in those results as well as experimental details and the angularly differential character of the partial cross sections are reported here. The experimental method used to obtain this information is completely new to the field of electron scattering. Its strengths and problems are discussed below in the context of describing the present experiment.

II. EXPERIMENTAL PRINCIPLE

The essence of the experimental method has been described in Refs. 5–7, and we will only reiterate it briefly here. Atoms in a magnetic field are initially prepared in a pure m_s' level of the $3S_{1/2}$ state by optical pumping, and some are then electron excited to the $3P_{3/2}(m_J)$ levels. The relative populations in these four Zeeman-split levels are measured by tuning through four spectrally resolved $3P_{3/2}(m_J)$-$5S_{1/2}$ transitions with a cw dye laser (designated ν_2), and detecting the 4P-3S, uv cascade fluorescence from the 5S state. This method and a typical ν_2-scan signal in the 218-G magnetic field are shown in Fig. 1. The area under each peak is proportional to the population of the corresponding $3P_{3/2}(m_J)$ level; the proportionality constants will be discussed in more detail below. These $3P_{3/2}(m_J)$ populations are in turn proportional to the $3S_{1/2}(m_s') \rightarrow 3P_{3/2}(m_J)$ (angle-integrated) partial cross sections, which can be reduced to the ratios of the $3S(m_s') \rightarrow 3P(m_s, m_L)$ partial cross sections. When these ratios are normalized to the previously measured total excitation cross section, the partial cross sections are obtained. The method of measuring dependences on electron scattering angle is described in the next paragraph.

When an electron scatters from a Na atom, it transfers momentum to the atom. Figure 2 illustrates how the outgoing direction (θ) of the inelastically scattered electron

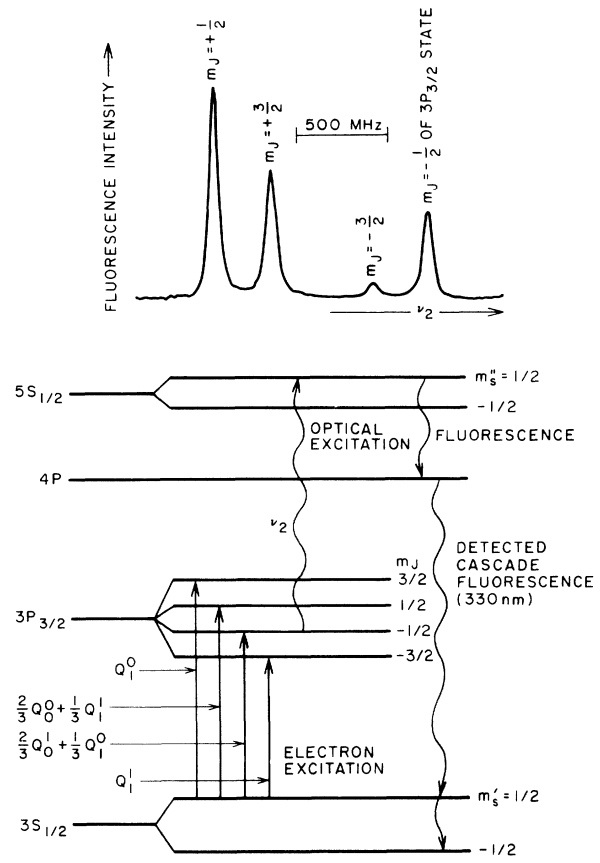

FIG. 1. Na energy levels and transitions involved in the experiment. Also a typical electron-excited ν_2 spectrum in the 218-G magnetic field is shown at the top of the figure.

is related to the recoil velocity of the atom. The atomic-recoil velocity component in the direction the ν_2 probe laser produces a Doppler shift of each $3P_{3/2}(m_J)$-$5S(m_s'')$ transition, so that the angular dependence of each partial cross section appears in the distribution of Doppler shifts for the four m_J transitions. The ν_2 laser beam counterpropagates with the electron beam, so that a Doppler recoil shift proportional to $\cos\theta$ is observed. The atom-electron mass ratio is very large, so this is a relatively small Doppler spread. Its observation is partially obscured by natural and residual atom-beam Doppler width, so the angular resolution is limited. As an example, inelastic $3S$-$3P$ excitation at 1 eV above threshold leads to a recoil red shift of 18 MHz for $\theta=0°$ and 66 MHz for $\theta=180°$. This 48-MHz spread compares to an experimental linewidth of ~25 MHz. However, the experimental resolution of response function is accurately measured by optically exciting $3S$-$3P$, so detailed angular information is obtained by a "deconvolution" procedure, in spite of this low ratio of recoil shift to experimental linewidth.

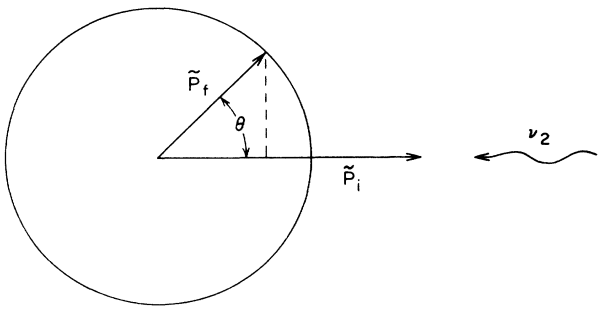

FIG. 2. Electron momentum diagram. The electron momentum change in the laser-beam direction, $P_i - P_f\cos\theta$, is transferred to the atom and detected as atomic-recoil Doppler shift.

III. EXPERIMENTAL DETAILS

A cross section of the experimental arrangement is shown in Fig. 3(a). A beam of sodium atoms deffuses from a recirculating oven, which is in a differentially pumped chamber. The beam is collimated to a thickness of 0.6 mm in the **B** (or **z**) direction and a width of 2.2 mm by a liquid-nitrogen-cooled slit, producing a residual Doppler full width at half maximum (FWHM) of ≈ 10 MHz. The atoms then enter a partially, magnetically shielded region, where the residual, z-directed magnetic-field strength is ~5 G. Here they are state selected into the $m_s'=\frac{1}{2}$, $m_I'=\frac{3}{2}$ sublevel of the $3S$ state by optical pumping with a circularly polarized laser beam (designated ν_1), and they remain in this sublevel as the atomic beam passes into the ~220-G field.

In the collision region some atoms are excited to the $3P_{3/2}$ state by the z-propagating electron beam, and some of these excited atoms are further excited to the $5S_{1/2}$ state before spontaneous emission by the overlapping, counterpropagating, ν_2 laser beam. (Electron and laser beams are ~2 mm diameter.) Approximately 20% of the 330-nm, $4P$-cascade fluorescence from $5S_{1/2}$ is collected by a spherical mirror and fused-silica lens, and detected by a photomultiplier [Fig. 3(b)]. Glass filters are used to block the (590-nm) $3P$ fluorescence and transmit the (330-nm) $4P$ fluorescence. The photoelectron pulses are collected by a data-acquisition system, which in turn is interfaced to a microcomputer which processes the data.

For the partial-cross-section data a ν_2 laser power of typically ~100 mW was used; on resonance this >90% saturated the $3P_{3/2}(M_J)$-$5S(M_S'',M_I'')$ transition and broadened each signal peak (Fig. 1) by 10–20 MHz. For the differential cross-section data a lower power was used and the instrumental linewidth of ~25 MHz was almost all due to the residual Doppler width (12 MHz) plus natural $3P$-$5S$ transition linewidth (13 MHz). The typical peak photoelectron signal rate was $\sim 10^4$/s in the former case and 4×10^3/s in the latter.

A. Spin alignment

In order to pump nearly all $3S_{1/2}$ atoms into the $(F',m_F')=(3,3)$ or equivalently the $(m_s',M_I')=(\frac{1}{2},\frac{3}{2})$ state, both ground-state hyperfine states are pumped using sidebands of a phase modulated ν_1 laser beam. This is done by tuning the laser to the midpoint between the $3S_{1/2}$ $F'=1$ and 2 to $3P_{1/2}$ $F=2$ transitions and passing

the beam though a $LiTaO_3$ crystal in a split-ring rf cavity[8] that it is modulated at ~886 MHz, corresponding to half of the $3S_{1/2}$ (zero-field) hyperfine splitting. To prevent drift of the ν_1 laser frequency, it is servolocked to the crossover resonance of an external Na saturated-absorption cell.

The degree of state selection was >92% into the $3S_{1/2}(m_s'=\frac{1}{2}, m_I'=\frac{3}{2})$ sublevel, and >96% for $3S_{1/2}(m_s=\frac{1}{2})$ spin selection, for the typical ~30 mW power at each hyperfine resonant frequency. This optical-pumping efficiency was measured in the interaction chamber by scanning the ν_2 laser across the $3S_{1/2}$-$3P_{3/2}$ and $3S_{1/2}$-$3P_{1/2}$ transitions with the ν_1 (optical-pumping) laser blocked and unblocked, and detecting the resultant $3P$ fluorescence. The residual population in each nearly emptied sublevel was obtained from the intensity change of the associated peak, i.e., since $\frac{1}{8}$ of the ground state is initially in each $3S$-state sublevel, the intensity ratio with and without optical-pumping yields the residual population in each of the seven partially emptied sublevels. Example spectra and dependences on experimental parameters are discussed elsewhere.[6,7,9]

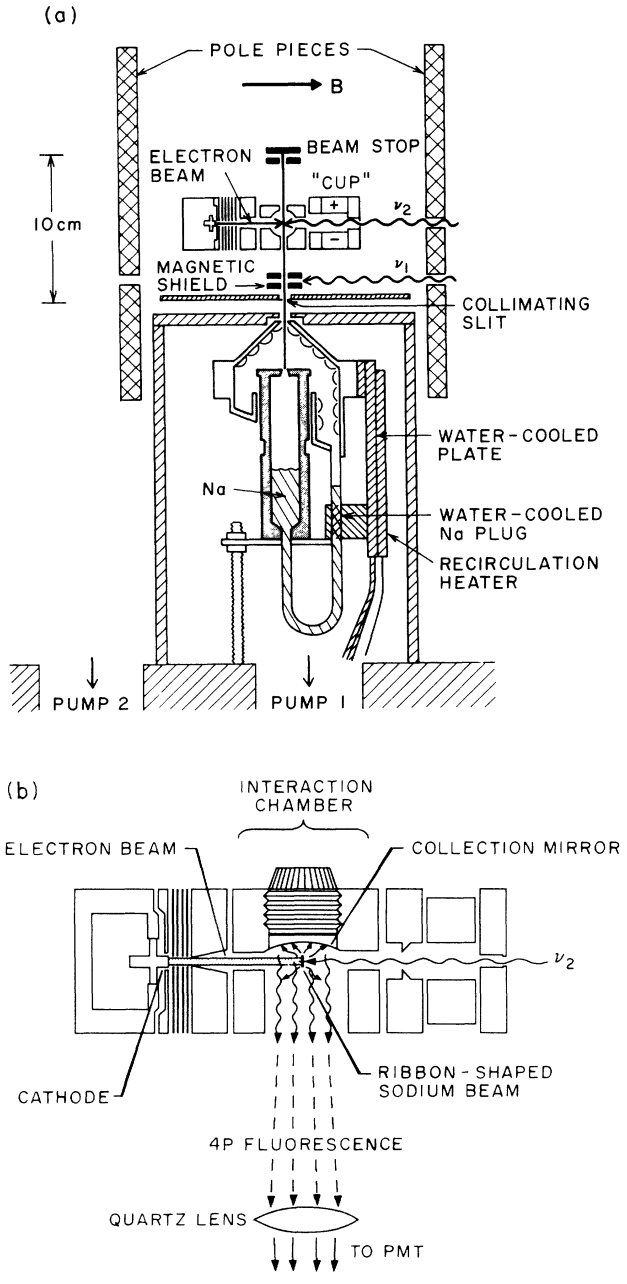

FIG. 3. Cross section of the apparatus (a) in the plane of the Na and electron beams and (b) in the plane of the detection optics and electron beams. The latter includes details of the electron gun. A fine Cu screen shielded the interaction region from possible charging of the insulating mirror surface.

B. Electron gun

A detailed cross-sectional view of the magnetically confined electron gum used in this experiment is shown in Fig. 3(b). An indirectly heated, ~1300-K alkaline-earth-oxide cathode, produces a beam thermal energy width of ~0.28 eV. The plates in front of the cathode are used to draw the electrons out from the cathode region with minimal transverse electric fields. Their 2.5-mm-diam apertures also define the beam size. These are followed by an element with tapered aperture to minimize lensing action as the electrons enter the larger bore of the interaction chamber.

The electron-energy width of our electron beam was indirectly checked by measuring the threshold shape of the $3P$-excitation cross section, which is the $3P$ polarization-corrected fluorescence in the absence of any laser beams. The present observed cross section was in excellent agreement with that observed in Refs. 10 and 11, indicating equivalent electron-beam energy spreads. The same type of cathode was used in all three experiments, and the beam-energy spreads were measured in Refs. 10 and 11 and found to be in agreement with the thermal spread. Thus, we believe that holds here as well. The effect of this energy spread on the analysis and results will be discussed in Sec. V.

The electron energy was established from the $3S$-$3P$ and $3S$-$4P$ excitation thresholds and the mean electron energy was varied by changing the voltage on the cathode V_K. The absolute energy in the interaction chamber sometimes varied by ~0.1 eV at fixed V_K over a period of a few hours. The interaction chamber was heated to ~150 °C to avoid Na buildup on its surfaces, so cathode-oxide changes and Ba coating of the nearby gun elements are the most likely causes for this drift. In order to determine the actual electron energy, the $3S$-$3P$ excitation function as a function of V_K was measured at frequent intervals between ν_2 scans.

A transverse-field electron collector was used to monitor the electron-gun current and prevent a return current from reentering the interaction chamber [Fig. 3(b)]. Here a strong transverse electric field produced an $E \times B$ drift of the electron's guiding center, and drove the electrons into the wall of the collector whose net current was measured by an electrometer.

C. Electron-beam spiraling

Electron spiraling occurs when the electrons acquire a velocity transverse to the confining magnetic field. If this occurs here the collision direction is not parallel to the quantization axis and the measured m_L dependences of the partial cross sections become mixed. Causes of transverse velocity are the thermal velocity of electrons emitted from the cathode and transverse electric fields arising from space charge, from nonuniform surface potentials due to alkaline-earth coatings on the electrodes, charging effects caused by oxide buildup on the electrodes, and lensing action arising from the finite-size holes of the accelerating plates causing deviations from equipotential planes.[12] Detailed consideration of these effects for our conditions, including electron-orbit calculations, are presented elsewhere.[7] These predict that typically Q_0^0 and Q_0^1 appear $\sim 2\%$ too small, Q_1^0 appears $\sim 9\%$ too large, and $Q_1^1 \sim 20\%$ too large.

The minimum degree of spiraling should occur when the electrons are drawn out with an approximately uniform electric field. This was confirmed by monitoring the near-threshold polarization of the fluorescence from the electron-excited $3P$ states. (This is $\sim 35\%$ in the 218-G field.) Minimum spiraling corresponds to a maximum in the ratio of $\Delta m_l = 0$ to $\Delta m_L = 1$ excitation, and hence a maximum in the observed polarization. By varying the electron-gun voltages, a broad maximum in the polarization was found when the electrons were weakly accelerated to $A3$, which was typically ~ 8 V above the cathode potential, and then decelerated from this ~ 6-eV energy to 2–6 eV used in the collision region. As described further below, our measured ratio of m_L cross sections was very close to that reported in Ref. 12, where an electrostatically confined electron beam free of spiraling was used.

D. Oven and beam density

The sodium atomic beam was produced by a recirculating oven, whose design is adapted from that of McClelland, Kelley, and Celotta,[4] based on a private communication. In normal operation, the water-cooled copper recirculating lid collects most of the sodium emanating from the 0.25-mm-diam orifice. A beam flag above the lid controls the passage of the beam into the downstream part of the apparatus. A water-cooled plug of solid sodium prevents the molten sodium in the oven reservoir from being pushed out through the recirculation tube by the Na vapor pressure. Following the completion of an experimental run the cooling water if turned off, then the plug and recirculation lid are heated to $\sim 200\,^{\circ}\mathrm{C}$, well above the melting point of sodium. The collected alkali metal then flows back into the oven.

This oven was designed to be used under either supersonic or effusive operating conditions. However, to avoid density-dependent radiation-trapping effects, while maintaining an approximately constant beam flux over the many hours of data collection, the oven was run as an effusive source for the data reported here. With periodic recirculation, it was operated for many hundreds of hours on its initial 30-g sodium charge.

The Na density in the interaction chamber was controlled to avoid radiation-trapping induced error, due to radiation from an electron-excited $3P_{3/2}(M_J)$ state exciting another atom to a different $3P_{3/2}(m_J)$ level. The essentially effusive atomic beam is Doppler broadened along its axis, but due to its collimation the self-absorption cross section $k(\nu)$ is much larger in the transverse directions. However $k(\nu)$ is lowered and very state specific due to the $3P$- and $3S$-state Zeeman splittings in the 218-G field (see Ref. 6). Since the $m_J = -\frac{3}{2}$ electron excitation cross section is only a few percent of the total it is particularly sensitive to radiation trapping. Thus, it is important to note that the dipole selection rule prevents radiative excitation of this state from the primary beam component, the $3S(m_s' = \frac{1}{2})$ state. After taking into account the radiation-angle-dependent reabsorption probability of the beam and the frequencies and polarization properties of the photons emitted in various decays, we conclude that radiation trapping should not be significant for the $n = 3\times 10^{10}$ cm^{-3} beam density normally used in the experiment.[6] To confirm this, a limited number of cross section scans were taken with approximately twice the above sodium density; the results were found to be in good agreement with the lower-density results. (The density is known from the integrated absorption in the optical-pumping region.)

The main chamber is pumped with an ion pump and fugitive Na vapor is pumped with a large (30×40 cm^2) copper sheet connected to a liquid-nitrogen-cooled cold finger, while the oven chamber is pumped by a turbo molecular pump. Typical operating background-gas pressures are $(1-5)\times 10^{-8}$ Torr.

E. Lasers

Two cw dye lasers, each with 1–2-MHz linewidth and ~ 100-mW total power were used for the 589-nm optical pumping and 616-nm, ν_2 excitation. As already noted, the optical-pumping laser was frequency locked using a Na saturated-absorption cell signal, and the ν_2 laser was scanned. For the partial (angle-integrated) cross section data an external confocal reference cavity with a 250-MHz free spectral range was used to monitor the linearity of the ν_2-laser scan. The measured deviations from linearity over the ~ 2 GHz scans were typically less than 10 MHz, and were largely taken into account in the data reduction. For the differential cross section data the ~ 200-MHz region around each peak was individually scanned, using a digital-frequency control method that attained ~ 1-MHz linearity and accuracy.[13] Lasers powers were controlled or monitored during all data accumulation.

IV. PARTIAL CROSS SECTIONS FOR m_s- AND m_L-CHANGING COLLISIONS

Angle-integrated partial cross section data were taken at nine electron-beam average energies E from 2.28 to 6 eV. Data equivalent to that in Fig. 1 were first reduced to the area under each of the four peaks. The ratios of

these areas were then reduced to the M_J dependence of the $3S(M_S=\frac{1}{2})\rightarrow 3P_{3/2}(M_J)$ partial cross sections, using the power-dependent sensitivity factors described in Appendix A and corrections for incomplete optical pumping. These three M_J-dependent ratios were then reduced to three ratios of $Q^{|\Delta m_s|}_{|\Delta m_L|}$ partial cross sections using the Clebsch-Gordan coefficient relationships shown in Fig. 1 [e.g., $Q(M_J=-\frac{1}{2})=(2Q^1_0+Q^0_1)/3$]. Here the four partial cross sections for m_s change Δm_s and m_l change Δm_l are denoted by $Q^{|\Delta m_s|}_{|\Delta m_L|}=Q^0_0$, Q^0_1, Q^1_0, and Q^1_1 and we make this reduction from (J,m_J) to $(m_l m_s)$ because the latter are more directly connected to the electron-collision process and calculations. The remaining parameters not determined in this experiment are the three relative phases between these four partial cross sections.

The total cross section Q_T for $3S$-$3P_{1/2}$ and -$3P_{3/2}$ excitation is the sum of all possible Δm_s- and Δm_L-changing cross sections:

$$Q_T=Q^0_0+Q^1_0+2Q^0_1+2Q^1_1 \ . \tag{1}$$

The $Q^{|\Delta m_s|}_{|\Delta m_L|}$ ratios obtained from the data by the above-described procedure are put on an absolute basis using Eq. (1). Since the shape of our measured total excitation cross section as a function of energy is in excellent agreement with the results of previous experiments,[10,11] we are able to assign to it absolute cross-section values, which we use to normalize the $Q^{|\Delta m_s|}_{|\Delta m_L|}$ ratios.

All four $Q^{|\Delta m_s|}_{|\Delta m_L|}$ cross sections were measured for energies below the (4.12 eV) $5S$ threshold, but the Q^1_1 cross section was not obtained from the $E>4.1$ eV data. The reason is that the ν_2 laser beam transfers population equally back and forth between the $3P_{3/2}(m_J)$ and $5S(m_s)$ levels, and as a result each peak signal is proportional to the difference between electron excitation of these $3P$ and $5S$ sublevels. The $3P$ excitation cross section is ~ 50 times larger than to $5S$ so this produces a very minor overall correction ($\sim 2\%$ for Q^0_0 and $\sim 5\%$ for Q^0_1 and Q^1_0). But the Q^1_1 component is only a few percent of the total $3P$ cross section, so this has a very major effect on the $m_J=-\frac{3}{2}$ or Q^1_1 components for energies above the $5S$ threshold. In fact, for $E>4.5$ eV the $5S(m_s''=-\frac{1}{2})$ cross section exceeds the $3P(m_j=-\frac{3}{2})$ cross section and we actually observe a decrease in $4P$ fluorescence as the ν_2 laser is scanned across this transition.

In order to correct the data for the incomplete optical pumping, the $3S$, $3P$, and $5S$ hyperfine eigenstates and energies in the 218-G magnetic field were calculated by diagonalization of the Hamiltonian matrix. The proportions of each (m_s,m_l) component in each of the partially emptied, intermediate-coupled $3S_{1/2}$ sublevels were calculated, and combined with the measured residual populations and the measured $Q^{|\Delta m_s|}_{|\Delta m_L|}$ ratios to iteratively correct the measured areas of the four ν_2-scan peaks. Since the $3S$-state m_s alignment was typically 95–98%, this is a few percent correction, except for obtaining Q^1_1 from the $m_J=-\frac{3}{2}$ peak where it is $\sim 50\%$ correction.

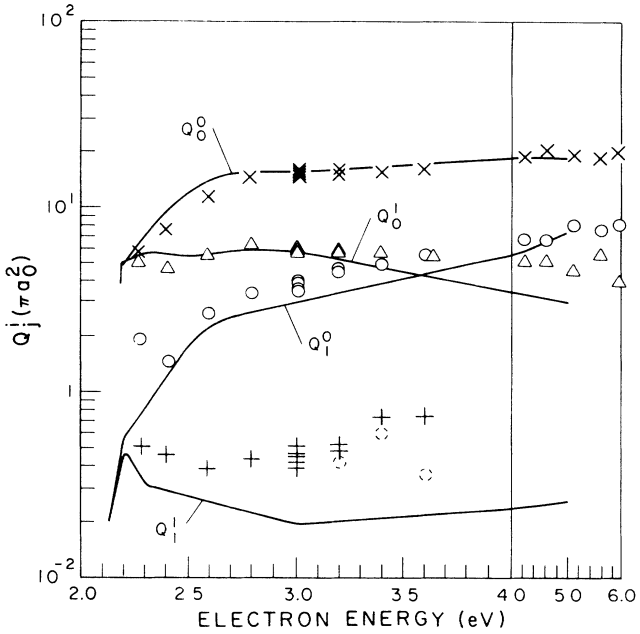

FIG. 4. Partial cross sections $Q^{|\Delta m_s|}_{|\Delta m_L|}$ for $3S\rightarrow 3P$ excitation with change $|\Delta m_s|$ and $|\Delta m_L|$ in the atomic electron vs electron energy. Note that the energy scale is contracted from 4–6 eV. Solid lines are drawn between the calculated points of Ref. 14. The $4S$ cascade corrected Q^1_1, based on the $Q^{|\Delta m_s|}_{4s}$ calculated in Ref. 15, are shown as broken circles above 3.2 eV.

These data, after corrections for ν_2-laser power dependence and normalization to the total $3S$-$3P$ cross section, are presented in Fig. 4.

Five measurements were taken at 3.0 eV as part of the power-dependence calibration discussed in the Appendix. The scatter in these points, shown in Fig. 4, is not correlated with the ν_2-laser power, indicating that the relative values of the $Q^{|\Delta m_s|}_{|\Delta m_L|}$ cross sections do not depend systematically on laser power. An estimate of random uncertainties, bassed on power-dependence measurements at 3.0 eV, ranges from $\pm 2\%$ for the larger Q^0_0 to $\pm 10\%$ for the smaller Q^1_1.

V. DIFFERENTIAL PARTIAL CROSS SECTIONS

As already noted, each of the four m_J peaks of the ν_2 spectrum (Fig. 1) is shifted and spread out due to the electron momentum change and resulting atomic recoil. A $3S\rightarrow 3P$ excitation accompanied by electron scattering into an angle θ produces a net ν_2 frequency shift of $(P_i-P_f\cos\theta)M\lambda$, where P_i and P_f are the electron momentum before and after the collision, M is the atomic mass, and λ the ν_2 wavelength (see Fig. 2). Since $d\nu_2\propto d(\cos\theta)$, each recoil spectrum is equivalent to $Q(\cos\theta)$ for that particular $|\Delta m_L|$ and $|\Delta m_s|$ partial component of the excitation cross section. In the present Na experiment this recoil frequency shift is 23 MHz $(\sqrt{E_i}-\sqrt{E_f}\cos\theta)$, where $E_i=E_f+2.1$ eV is the electron collision energy in eV. For the present measurements, the final electron energy E_f varied from 0.5 to 1.5 eV, and the Doppler-shift difference between 0° and 180°

electron scattering varied from 33 to 56 MHz. In comparison, the experimental linewidth without any recoil was ~25 MHz, due to residual beam Doppler spread, plus natural and power broadening of the $3P$-$5S$ transition. Thus, to obtain meaningful angular resolution, it is essential to reduce the instrumental smearing of the recoil distribution. The basic idea of the method chosen for this will first be briefly described, then details will be given.

The atomic-recoil Doppler spectrum for each m_J line was measured relative to its unshifted position by alternately electron and optically exciting the $3P_{3/2}$ state. An example of such data, for the $m_J=\frac{3}{2}$ component, is shown in Fig. 5. If the instrumental width were negligible and complete optical pumping were achieved, the electron-excitation signal $S(\Delta\nu_2)$ in Fig. 5 would equal $Q(x)$, where $\Delta\nu_2=(23\text{ MHz})(\sqrt{E_i}-\sqrt{E_f}x)$, $\Delta\nu_2$ is measured from the optical-excitation signal, and $x=\cos\theta$. The $Q(x)$ corresponding to this signal, obtained from the analysis described below, is labeled Q in Fig. 5. This $Q(\Delta\nu_2)$ is bounded by $\Delta\nu_2=18$ and 62 MHz relative to the "no-recoil" center of the optical-excitation peak, corresponding to $x=+1$ or -1 or $\theta=0°$ and 180°.

The first step to reducing the data to $Q(x)$ is to correct for incomplete optical pumping. Most of each signal in Fig. 5 is due to ν_2 excitation from the $m_J=\frac{3}{2}$, $M_I=\frac{3}{2}$ sublevel of the $3P_{3/2}$ state, since the Na beam was initially highly optically pumped into the $m_s=\frac{1}{2}$, $m_I=\frac{3}{2}$ sublevel of $3S_{1/2}$ and electron excitation does not change m_I. However, there is a small contribution to each signal in this figure, due to $m_J=\frac{3}{2}$, $m_I\neq\frac{3}{2}$ sublevels that result from the incomplete optical pumping. The size and positions of these small (<5%) contributions have been calculated from knowledge of the residual $3S_{1/2}$ sublevel populations and the energies of the $3P_{3/2}$ and $5S_{1/2}$ sublevels. In the optical-excitation case, intermediate-coupling radiative transition probabilities were used, and

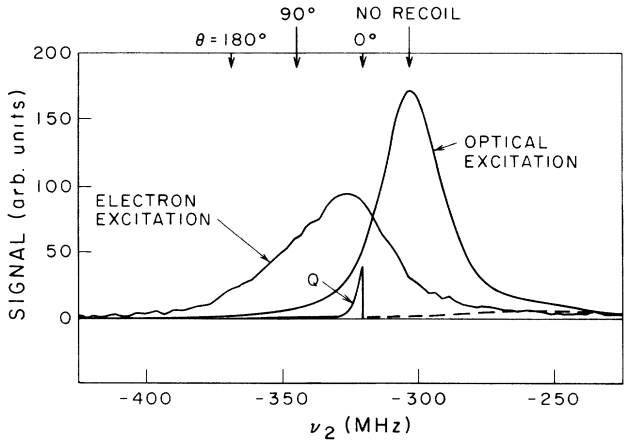

FIG. 5. 330-nm fluorescence vs ν_2 for optically excited and (3.1-eV) electron-excited $3P_{3/2}$ state atoms. The ν_2 transition from the $3P_{3/2}$, $m_J=3/2$ state is shown. The dashed line is the contribution of undesired $3S_{1/2}(F',m_F')$ levels to the optically excited signal, due to incomplete optical pumping. The line labeled Q is the recoil spectrum or $Q(\cos\theta)$, as it would appear in the absence of instrumental broadening.

in the electron case the relative sizes of the $3S_{1/2}(m_J)\rightarrow 3P_{3/2}(m_J)$ cross sections from the previous section (Fig. 4) were used to establish the relative sizes of different contributions. These $m_I\neq\frac{3}{2}$ contributions to the optical-excitation signal are shown as a dashed line in Fig. 5; each contribution has been given the same $\Delta\nu_2$ shape as the primary signal for their m_J sublevel. These are subtracted from the experimental signals to obtain the single-component $S(\Delta\nu_2)$ and $I(\Delta\nu_2)$.

The imperfect optical-pumping correction is small for the peaks labeled $m_J=\frac{3}{2}$, $\frac{1}{2}$, and $-\frac{1}{2}$ in Fig. 1, and they are all analyzed as described in the previous paragraph. However, for the peak labeled $m_J=-\frac{3}{2}$ the normal $m_J=-\frac{3}{2}$, $m_I=\frac{3}{2}$ component results from the very small Q_1^1 partial cross section (Fig. 4), whereas the overlapping contributions due to incomplete optical pumping include contributions from the other much larger Q_l^j. Thus, in addition to being the smallest peak, major corrections would be needed to analyze this peak; it has not been analyzed in this work.

The next step in the data reduction is to remove the effect of instrumental broadening, insofar as is possible. The actual experimental electron-excitation signal $S(\Delta\nu_2')$ is a convolution of $Q(\Delta\nu_2)$ with the instrument function $I(\Delta\nu_2-\Delta\nu_2')$, where the optical-excitation signal is the instrument function

$$S(\Delta\nu_2')=\int Q(\Delta\nu_2)I(\Delta\nu_2-\Delta\nu_2')d(\Delta\nu_2)\ . \tag{2}$$

A formally simple way to invert Eq. (2) to obtain $Q(\Delta\nu_2)$ from the data, after removal of incomplete-optical-pumping contributions, would be to use Fourier deconvolution. However, this does not work very well here because the $Q(\Delta\nu_2)$ function in Eq. (2) is finite within the $\Delta\nu_2=18$–62-MHz range and zero elsewhere. To reproduce the resulting steps in $Q(\Delta\nu_2)$ at these two frequencies requires very high "frequency" Fourier components, thereby accentuating experimental noise and obscuring the results. Consequently, we have "inverted" Eq. (2) by least-squares fitting to a parametrized $Q(\Delta\nu_2)$ that is zero outside the allowed range. We initially chose $Q(x)=\sum_l C_l P_l(x)$, where $P_l(x)$ are the Legendre polynomials, and we obtain the constants C_l by the least-squares fitting. The sum was extended from $l=0$ to $l_{\max}=2$, 3, 4, etc., and the resulting $Q(x)$ convergence was noted. For some m_J, E_f cases, where $Q(x)$ was more or less evenly distributed between $x=\pm1$, good convergence was obtained in this way. But for some cases $Q(x)$ is highly peaked at small angles ($x\sim1$), and the Legendre expansion then converges poorly and oscillates rapidly at $x<0.5$. We therefore added to the $Q(x)$ Legendre expansion an exponential term, of amplitude A_+ at $x=1$ and which exponentially decreases with decreasing x. The width of the exponential function was chosen to roughly match the forward peak obtained from the Legendre expansion alone, but this was not critical to the final $Q(x)$ as the Legendre terms compensate for moderate changes in the width of the exponential, i.e.,

$$Q(x)=\sum_{l=0}^{l_{\max}} C_l P_l(x)+A_+\exp[(x-1)/\Delta]\ . \tag{3}$$

In a few m_J-peak, E_f cases the Legendre expansion alone also indicated a major backward peak; in these cases the sign of x in the exponent was reversed to add a backward-peaked exponential.

The next detail involves the instrument function used in the least-squares fitting routine. The optical-excitation signal was easily made large and relatively noise free, allowing an analytic form to be accurately fitted to this measured $I(\Delta\nu_2-\Delta\nu_2')$, after making minor corrections for incomplete optical pumping. $I(y)$ was well fitted by a Voigt function, with comparable size Gaussian and Lorentzian parts and slightly different parameters for positive and negative y. This minor asymmetry was attributed to slightly nonorthogonal atomic and laser-beam directions.

Another small but important correction was to subtract the overlapping wings of the different m_J peaks (Fig. 1). Each peak was also scanned individually several times and the data were averaged. To minimize power broadening, the total laser power density was ~ 8 mW/cm^2 for the $m_J=\pm\frac{1}{2}$ peak and $\frac{1}{3}$ of this for the $m_J=\frac{3}{2}$ peak, to adjust for the different probe-transition strengths. Other details can be found in Ref. 6.

Differential cross-section data were taken at average electron-collision energies of 2.6, 3.1, and 3.6 eV. (The electron-beam FWHM is ~ 0.28 eV.) In Fig. 6 we show the shape of the three $S(\Delta\nu_2)$ signals at each energy, after corrections for imperfect optical pumping and overlapping wings. These signals are normalized here to equal area and shifted to place $\Delta\nu_2=0$ at $\theta=90°$ or $x=0$. Considering Fig. 6(b) as an example, it is apparent that the $m_J=-\frac{1}{2}$ peak is nearly symmetric about $x=0$ and widely spread, reflecting a $Q(x)$ that must be relatively constant between $x=-1$ and 1 (i.e., isotropic scattering). In contrast, the $m_J=\frac{3}{2}$ peak is strongly weighted toward small angles, indicating a $Q(x)$ that is sharply peaked at $x=1$. The $m_J=\frac{1}{2}$ signal is similarly forward peaked, but with a slower falloff toward $x=-1$, indicating a $Q(\theta)$ that also has a sharp $x=1$ peak but accompanied by some larger-angle contributions. It is these differences between $S(\Delta\nu_2)$ shapes in Fig. 6(b) that produce the very different $Q(\theta)$ when we least-squares fit to Eq. (3) in Eq. (2). The $Q(x)$ that have resulted from this fitting are shown in Fig. 6 below the $S(\Delta\nu_2)$; they are consistent with this discussion. We will now give examples of how these were obtained, choosing different m_J and E_i for each example.

In Fig. 7 we give an example of the fitting procedure used to obtain the various $Q(x)$ from the data. Here the experimental signal $S_E(\Delta\nu_2)$ for the $m_J=\frac{1}{2}$, $E_i=3.1$ eV case is compared to two fitted signals $S(\Delta\nu_2)$ in part (a). Residuals $S_E(\Delta\nu_2)-S(\Delta\nu_2)$ are shown in part (b) for the better fit in (a) and an improvement on this. Equation (3) in Eq. (2), with the above relation between x and $\Delta\nu_2$ and the $L_{\max}$ indicated, has been used to least-squares fit the parameters in Eq. (2) to obtain the fitted signals. The $Q(x)$ from these least-squares fits are shown in part (c) and (d). These were obtained using the form of $Q(x)$ in Eq. (3), while truncating the Legendre expansion at $L_{\max}$ and taking $A_+=0$ for Fig. 7(c) and including the ex-

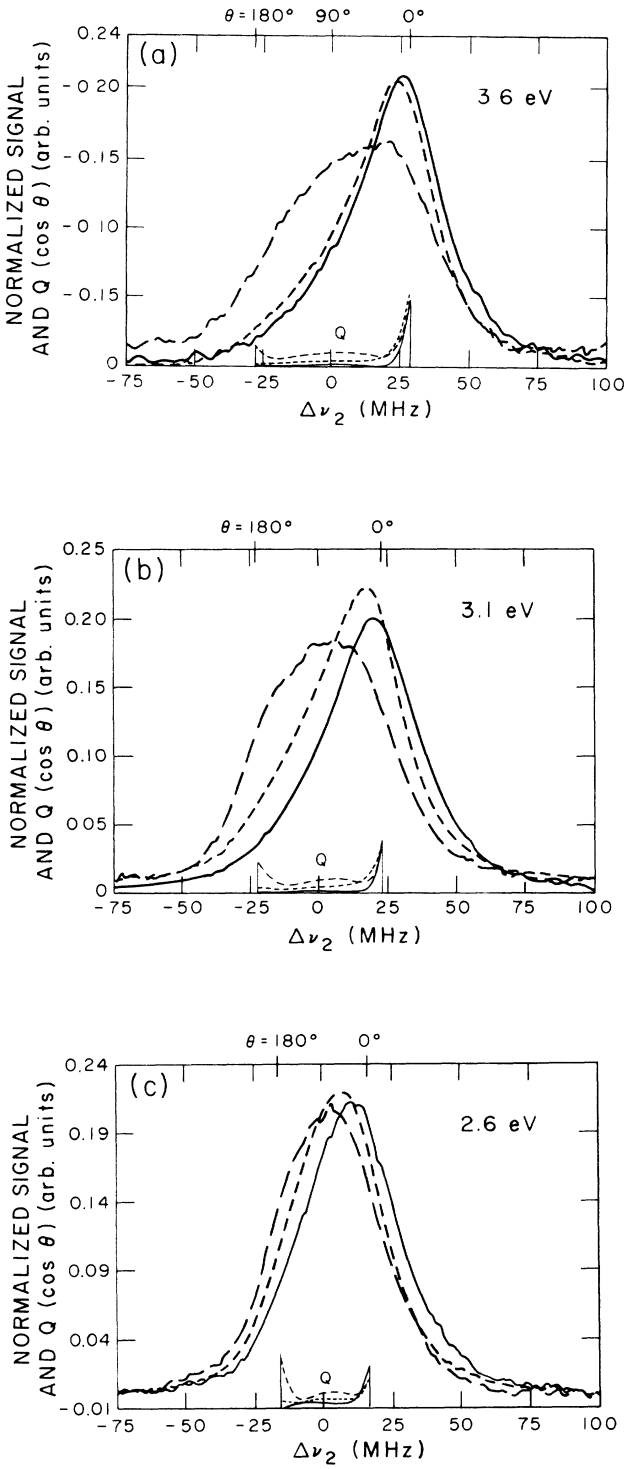

FIG. 6. 330-nm fluorescence signal vs $\Delta\nu_2$ for three electron energies and three of the m_J peaks shown at the top of Fig. 1. The solid line is for the $m_J=\frac{3}{2}$ peak, the short-dashed line for the $m_J=\frac{1}{2}$ peak, and the long-dashed line for the $m_J=-\frac{1}{2}$ peak. Here the signals have been shifted to place 90° scattering at 0 detuning and normalized to equal areas. The differential cross sections $Q(\cos\theta)$ are plotted below, at the detuning where they would appear in the absence of experimental broadening.

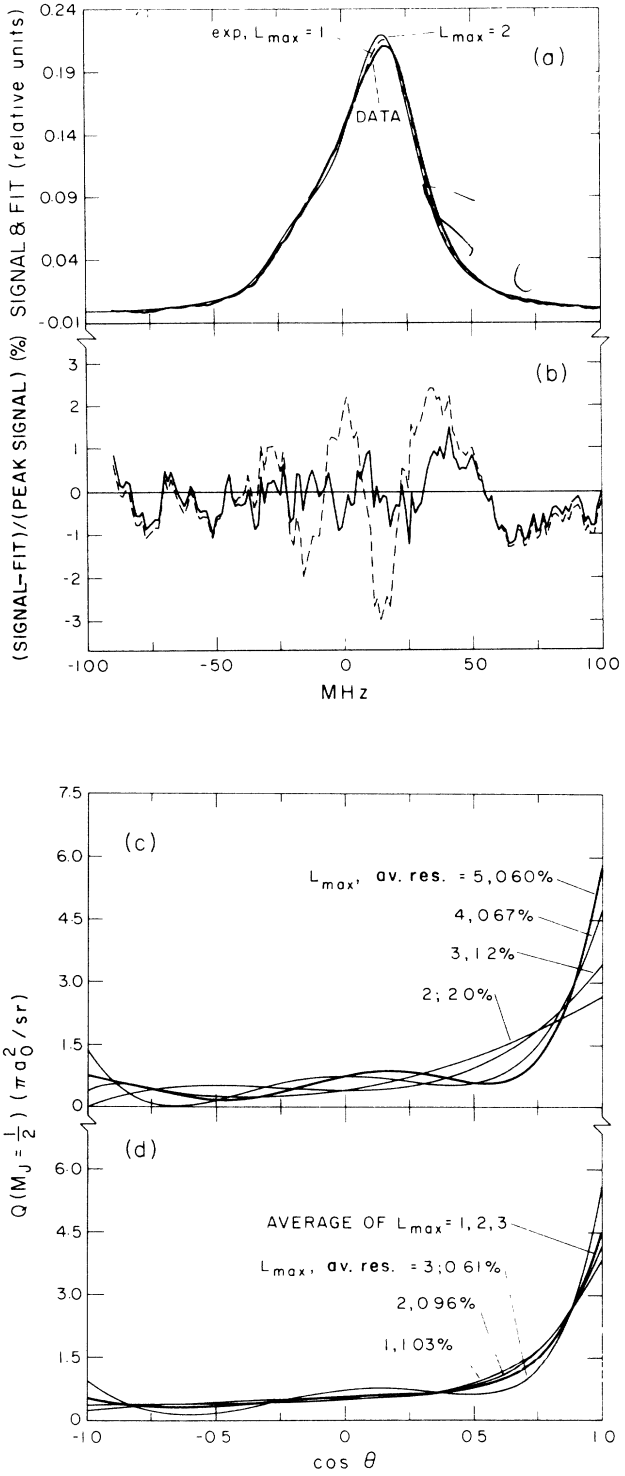

FIG. 7. Analysis of the $m_J=\frac{1}{2}$, $E_i=3.1$-eV data. (a) Comparison of data, corrected for incomplete optical pumping, to a least-squares fit using Eq. (3) in Eq. (2), in one case with $L_{max}=2$ and no exponential term, and in the other using $L_{max}=1$ plus the exponential. (b) Residuals between the data and least-squares fits using the exponential term and $L_{max}=1$ (dashed line) and $L_{max}=3$ (solid line). (c) $Q(x)$ for the L_{max} shown, from least-square fits without the exponential term in Eq. (2). Average fractional residuals are also given for each case. (d) Same as (c) but including the exponential term.

ponential term in the fits of Fig. 7(d).

Note that as L_{max} increases in Fig. 7(c), the $Q(x)$ becomes increasingly forward ($x=1$) peaked, and they also oscillate strongly at small-x values due to the oscillatory character of Legendre polynomials. Further increasing L_{max} causes these oscillations to yield nonphysical negative $Q(x)$ between $x=-1$ and 0. This is an inadequacy of the truncated Legendre expansion in trying to fit a sharply peaked $Q(x)$. Nonetheless, the overall pattern of the various $Q(x)$ in Fig. 7(c) is consistent for $x<0.5$, suggesting that the "best" $Q(x)$ passes smoothly through the middle of their oscillations, then follows the $L_{max}=4$ or 5 curves from $x=0.5$ to 1.0. This indication is tested in Fig. 7(d), where the exponential term is included in the $Q(x)$ expansion with A_+ fixed by the least-squares fitting, and the Legendre terms no longer have to produce the sharp forward peak. Note that the oscillations are now considerably reduced for $x<0.5$, and the average $Q(x\le 0.5)$ in Fig. 7(d) is very close to the average of the $Q(x\le 0.5)$ in Fig. 7(c). Furthermore, the $L_{max}=3$ curve in Fig. 7(d) is very close to the $L_{max}=5$ case in Fig. 7(c); two very different fitting procedures converged to essentially the same $Q(x)$ and average residuals. Thus, we conclude that the actual $Q(x)$ for this m_J, E_f case is effectively bounded by the "average" and $L_{max}=3$ curves in Fig. 7(d). Note, in Fig. 7(b), that large residuals occur in the +60- to 80-MHz region for the optimum fits. This is probably due to small imperfections in the incomplete-optical-pumping corrections to $I(\Delta\nu_2)$. The fact that the average fractional residuals,

$$\bar{R}=\left[\sum_{n=1}^{N}[S_E(\Delta\nu_n)-S(\Delta\nu_n)]^2\right]^{1/2} N^{-1}S(0)^{-1}\,, \tag{4}$$

are only ~0.6% in spite of this minor problem indicates excellent convergence of this least-squares fitting.

We will now give a different example of the sensitivity of the data fitting to the shape of $Q(x)$, using $m_J=\frac{3}{2}$, $E_i=3.6$ eV data. In Fig. 8 we show $S_E(\Delta\nu_2)$ and two $S(\Delta\nu_2)$, corresponding to the two $Q(x)$ shown. The solid-line $Q(x)$ with the low-amplitude tail extending to $x=-1$ was obtained by least-squares fitting to Eq. (3), with $L_{max}=3$ and the exponential included. The other, dashed-line $Q(x)$ is a pure exponential, with the same $Q(1)$ and a width that produces the same area. Thus, we are comparing the optimally fitted $Q(x)$ to a forward-peaked exponential, in order to show the sensitivity of the fit to the low amplitude, high-angle "tail." As seen in Fig. 8 there is a very large difference in the fit, demonstrating that the data are quite sensitive to such differences in $Q(x)$.

The third example, $E_i=2.6$ eV and $m_J=-\frac{1}{2}$, will be used to describe a slightly modified reduction that was used for the $m_J=-\frac{1}{2}$ data. Since $Q(m_J=\frac{3}{2})=Q_1^0$, the analysis of the $m_J=\frac{3}{2}$ peak directly yields $Q_1^0(x)$. Also $Q(m_J=\frac{1}{2})=\frac{2}{3}Q_0^0+\frac{1}{3}Q_1^1$ and $Q_1^1/Q_0^0\cong 0.01$, so analysis of the $m_J=-\frac{1}{2}$ peak yields $Q_0^0(x)$. On the other hand, $Q(m_J=-\frac{1}{2})=\frac{2}{3}Q_0^1+\frac{1}{3}Q_1^0$ and $Q_0^1/Q_1^0=1$ to 2 in the 2.6–3.6-eV range (Fig. 4). Since $Q_1^0(x)$ has already been established from the $m_J=\frac{3}{2}$ analysis, we wish to obtain $Q_0^1(x)$ from the $m_J=-\frac{1}{2}$ peak. This has been done by

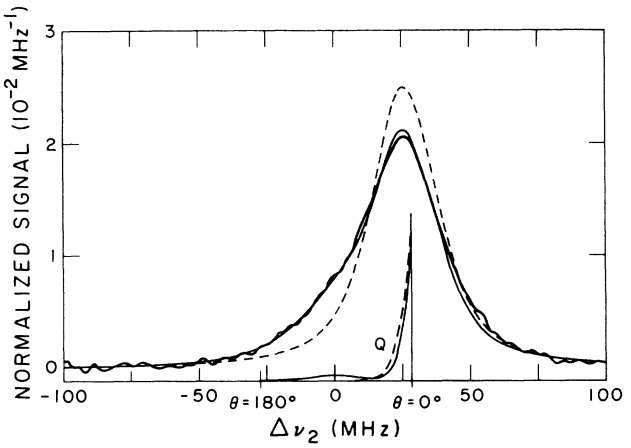

FIG. 8. Measured $S_E(\Delta\nu_2)$ and calculated $S(\Delta\nu_2)$ signals for the $m_J=\frac{3}{2}$, $E_i=3.6$ eV data. The two $Q_0^0(x)$ shown yield the $S(\Delta\nu_2)$ fits. The solid line Q_0^0 is the optimum exponential plus Legendre-polynomial fit, while the dashed line Q_0^0 is a pure exponential.

first subtracting $S_1^0(\Delta\nu_2)/3$ from $S(\Delta\nu_2)_{m_J=-\frac{1}{2}}$, then fitting the residual, $\frac{2}{3}S_0^1(\Delta\nu_2)$, to obtain $Q_0^1(x)$. Here $S_1^0(\Delta\nu_2)$ is $\frac{1}{3}$ of the measured $S(\Delta\nu_2)_{m_J=3/2}$, where the factor of $\frac{1}{3}$ is due to the different Clebsch-Gordan coefficients of the $3P_{3/2}(m_J)$-$5S(m_s)$ transitions. Figure 9 shows this procedure for the $E_i=2.6$ eV data. The $Q_0^1(x)$ least-squares fit to $S_0^1(\Delta\nu_2)$ was done with and without a backward-peaked exponential in Eq. (3) and versus $L_{\max}$. These $Q_0^1(x)$ versus $L_{\max}$ are shown in Fig. 9(b), and the final fit to $S_0^1(\Delta\nu_2)$ is shown in Fig. 9(a). Here we only present $Q(x)$ obtained without the backward-peaked exponential, showing that excellent convergence was obtained even with this simpler expansion. The $Q_0^1(x)$ in Fig. 10 is an average of the $L_{\max}=2$, 3, and 4 curves in Fig. 9(b). For all E_i a $Q(x)$ fitted to $S(\Delta\nu_2)_{m_J=-1/2}$ showed forward and backward peaks, whereas a $Q(x)$ fitted to $S_0^1(\Delta\nu_2)$ showed no forward peak, i.e., the forward peak is entirely due to the $\frac{1}{3}Q_1^0$ part of the $m_J=-\frac{1}{2}$ cross section.

$Q(x)$ and $\bar{R}$ values for the full array of $L_{\max}$, with and without the exponential term, are given in Ref. 6 for all m_J, E_i cases and are not repeated here. They systematically support the optimuum $Q(x)$ shown in Figs. 6 and 10. These $Q(x)$ are given by Eq. (3) with $\bar{C}_l$ in place of C_l, where $\bar{C}_l$ is obtained by averaging the C_l from the higher $L_{\max}$ fits. This averages through minor oscillations that varied randomly with $L_{\max}$, and follows the higher-$L_{\max}$ fits to the forward peak, as shown in the Fig. 7(c) example. The accuracy of these $Q(x)$ shapes across Δx differences of ≥ 0.5 is believed to be good, perhaps 10%, whereas we cannot easily distinguish much larger fluctuations with a small Δx period. For this reason it is not feasible to assign a fractional uncertainty to these $Q(x)$; shape changes are highly correlated. For example, areas under the forward peaks, relative to $Q(x<0.5)$, are probably of 10% accuracy, whereas the steepness of the forward-peak falloff is highly uncertain. The data should be thought of as fixing the overall shape but not the fine structure of $Q(x)$. In addition, the $Q_0^1(x)$ are less accurate near $x=1$ since a much larger $Q_1^0(x)$ contribution has been subtracted from the measured $m_J=-\frac{1}{2}$ signal (see Fig. 10).

The electron energy spread of ~ 0.28 eV typically causes $\sim$1-MHz spread in the recoil frequency shift for $\theta=0°$ and $\sim$4-MHz spread for $\theta=180°$. [Recall that $\Delta\nu=(23\text{ MHz})\,(\sqrt{E_i}-\sqrt{E_f}\cos\theta)$.] This corresponds to a spread of $\cos\theta$ of ~ 0.02 at $\theta=0°$ and ~ 0.08 at 180°. The fitting procedure largely compensates for this relatively minor spread in the data, particularly as the resulting Q do not change this rapidly. (Note, in Fig. 10, that the narrowest forward peaked $Q(\cos\theta)$ has a half-width of ~ 0.08 and the narrowest backward-peaked case has ~ 0.14 half-width.) Thus, the primary effect of the energy spread is to average over any rapid energy dependences, just as in other collision experiments.

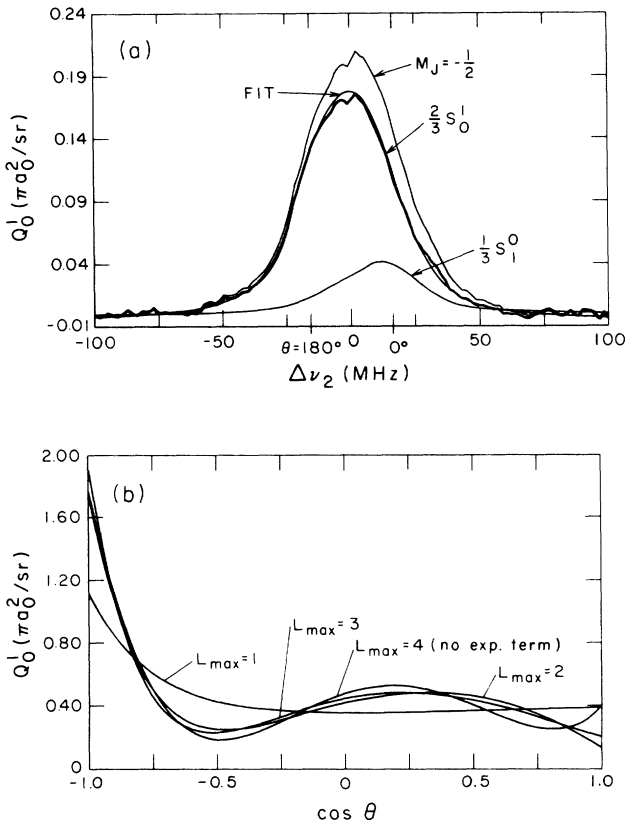

FIG. 9. Analysis of the $m_J=-\frac{1}{2}$, $E_i=2.6$ eV data. (a) The measured $S_E(\Delta\nu_2)$ is labeled $M_J=-\frac{1}{2}$; this results from $\frac{2}{3}Q_0^1+\frac{1}{3}Q_1^0$. The $S_1^0(\Delta\nu_2)$ contribution to the data is labeled $\frac{1}{3}S_1^0$; this is subtracted from $S_E(\Delta\nu_2)$ to produce the $S_0^1(\Delta\nu_2)$ curve labeled $\frac{2}{3}S_0^1$. The "fit" or calculated $S_0^1(\Delta\nu_2)$ corresponds to any of the $Q_0^1(x)$ shown in (b) other than the $L_{\max}=1$ curve. The $Q_0^1(x)$ in (b) are least-square fits using a backward-peaked exponential plus Legendre polynomials for the $L_{\max}=1$–3 case and only Legendre polynomials for the $L_{\max}=4$ case. The fractional residuals $\bar{R}$ are 1.42% for the $L_{\max}=1$ case and 1.26% for the other cases.

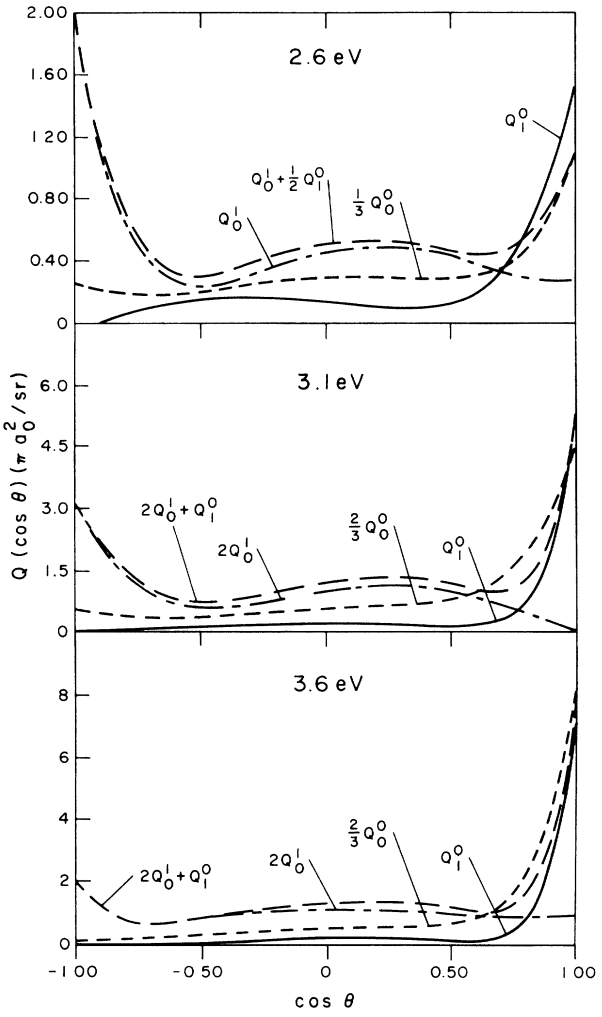

FIG. 10. Differential cross sections $Q^{|\Delta m_s|}_{|\Delta m_L|}(\cos\theta)$ at three energies, obtained from the data analysis. These are shown using multiplicative factors for improved visibility, and the long-dashed curve is proportional to $Q_{m_J=-1/2}(\cos\theta)$.

VI. DISCUSSION

A. Partial cross sections

Our $3P$-excitation data are compared to the calculation of Moores and Norcross[14] in Fig. 4, but the data include effects of cascading from higher-lying states for electron energies above the respective thresholds. The first of these states is $4S$, with a threshold energy of 3.19 eV. Electrons are excited from $3S(m_s'=\frac{1}{2})$ to $m_s''=\frac{1}{2}$ or $-\frac{1}{2}$ of the $4S$ state with cross sections $Q^{|\Delta m_s|}_{4S}=Q^0_{4S}$ or Q^1_{4S}, respectively. Atoms in the $4S$, m_s'' state radiatively decay to $3P(m_L,m_s'')$ states with approximately equal probability for $m_l=1,0,-1$, the slight deviation from strict equality being due to the intermediate coupling in the magnetic field. Therefore, the direct $3S$-$3P$ cross section $Q^{|\Delta m_s|}_{|\Delta m_L|}$ is related to the measured $3S$-$3P$ cross section $\tilde{Q}^{|\Delta m_s|}_{|\Delta m_L|}$ by

$$Q^{|\Delta m_s|}_{|\Delta m_L|}\simeq\tilde{Q}^{|\Delta m_s|}_{|\Delta m_L|}-\tfrac{1}{3}Q^{|\Delta m_s|}_{4S}\ . \tag{4}$$

Mitroy[15] has calculated $Q^{|\Delta m_s|}_{4S}$ cross sections at several energies between 3.26 and 4.1 eV, using a four-state close-coupling approach. We have used these results to make the cascade corrections shown in Fig. 4. At 3.55 eV, for instance, cascading from the $4S$ state contributes $0.4\pi a_0^2$ to Q^0_0 and Q^0_1, and $0.3\pi a_0^2$ to Q^1_0 and Q^1_1. This is a small fractional correction to all but Q^1_1.

The effect of cascading from higher-lying states, particularly $3D$ at 3.62 eV, is less certain. Phelps and Lin[16] have measured the total cross sections Q for electron excitation of many states in sodium, but they did not measure the partial cross sections for excitation into the m_L and m_s components. In the absence of such information, we can estimate the cascade contributions by assuming that the six (m_L,m_s) levels of $3P$ are equally populated by the radiative decay from $3D$. At an energy of $\sim$4 eV, Phelps and Lin report $Q=4\pi a_0^2$ for $3S\rightarrow 3D$ excitation, so this yields $\sim 0.7\pi a_0^2$ cascade into each $Q^{|\Delta m_s|}_{|\Delta m_L|}$. However, the measured total Q^1_1 is only $\sim 0.5\pi a_0^2$ at this energy, so the uncertainty in how the $3D$ excitation is distributed among the $3D(m_L,m_s)$ levels leads to a very major uncertainty in directly excited Q^1_1. The other $3S$-$3P$ partial cross sections are much larger, so that this is only a 5% to 10% contribution.

Phelps and Lin also report $0.9\pi a_0^2$ for the $3S$-$4P$ excitation cross section at 4 eV. About $\frac{2}{3}$ of the $4P$ atoms decay through the $4S$ state to $3P$, while most of the remainder contribute to the observed 330-nm fluorescence. The latter increases the overall background signal and hence noise, but does not affect our signal shape as the ν_2 laser is scanned. All initial alignment and most of the spin orientation of the $4P$ state is lost in the $4P$-$4S$-$3P$ cascade processes, so to a good approximation the m_L and m_s levels of $3P$ are equally populated, and the correction will have the form of Eq. (4), with $Q_{4S}/3$ replaced by $2Q_{4P}/9$, or $0.2\pi a_0^2$ at 4 eV.

Direct excitation of $5S$ for $E>4.1$ eV leads to an interesting experimental complication. When the ν_2 laser is tuned to a $3P_{3/2}(m_J)$-$5S_{1/2}(m_s'')$ transition, the population difference between these levels is decreased. Thus, the difference between direct excitation of $3P_{3/2}(m_J)$ and $5S_{1/2}(m_s'')$ is observed. Again, the $3P_{3/2}(m_J=\frac{3}{2},\frac{1}{2},-\frac{1}{2})$ states all have electron-excitation cross sections much greater than that for excitation to either of the $5S_{1/2}(m_s'')$ states, so $5S$ electron excitation does not significantly affect the experimentally determined Q^0_0, Q^1_0, and Q^0_1. However, the cross section for excitation to $3P_{3/2}(m_J=-\frac{3}{2})$, proportional to Q^1_1, is somewhat less than that for excitation of $5S_{1/2}(m_s''=-\frac{1}{2})$ above 4.1 eV, and we actually observe a decrease in the observed $4P$ fluorescence as the ν_2 laser is scanned across this transition (see Ref. 6).

Summarizing these cascade effects, they produce $<5\%$ correction to Q^0_0, and $<10\%$ to Q^1_0 and Q^0_1. However, cascade corrections cannot be reliably made to Q^1_1 at $E>3.6$ eV, and the data in Fig. 4 must be considered as a sum of direct plus unknown cascade contributions. From $E=3.2$–3.6 eV a cascade-corrected Q^1_1 is shown, based on Mitroy's calculation of $Q^{|\Delta M_s|}_{4s}$.

Previously published preliminary results from our experiment were taken over a more restricted energy range and not fully corrected for incomplete optical pumping.[5] Although the present data are more complete and reliable, the earlier data are consistent.

In Fig. 11, we plot the measured "reduced" polarization $P=(Q_0-Q_1)/(Q_0+Q_1)$, where $Q_0=Q_0^0+Q_0^1$, and $Q_1=Q_1^0+Q_1^1$. This represents the polarization that would be observed if there were no fine or hyperfine interactions, which partially depolarize the atoms between the time of excitation and subsequent fluorescent decay.[17] Also shown on the plot are the reduced polarization values calculated by Moores and Norcross[14] (without cascade corrections), and a curve representing the average experimental data of Enemark and Gallagher.[11] Electron spiraling will lower the polarization measured with our magnetically confined gun, and as expected our results are slightly lower than the theoretical values and the measurements of Enemark and Gallagher using an electrostatic gun. The polarization measured here is generally consistent with several percent degradation due to spiraling; this is somewhat larger than expected from considerations of the mechanisms described in Sec. III C, which are thought responsible for inducing the spiraling.[7] The inconsistent near-threshold polarization value at 2.28 eV is attributed to minor energy drift and/or background drift during the >1 hour data-averaging required for this near-threshold condition.[7] This uncertainty reduced to $<3\%$ for $E\geq 2.5$ eV; the signal-to-random-noise ratio for all the ν_2-scan peak-area measurements had a typical statistical uncertainty of $\sim 1\%$. Additional uncertainties arising from determination of the baseline and line overlap are estimated as $<5\%$ for Q_1^1 and $\sim 1\%$ for the other partial cross section.

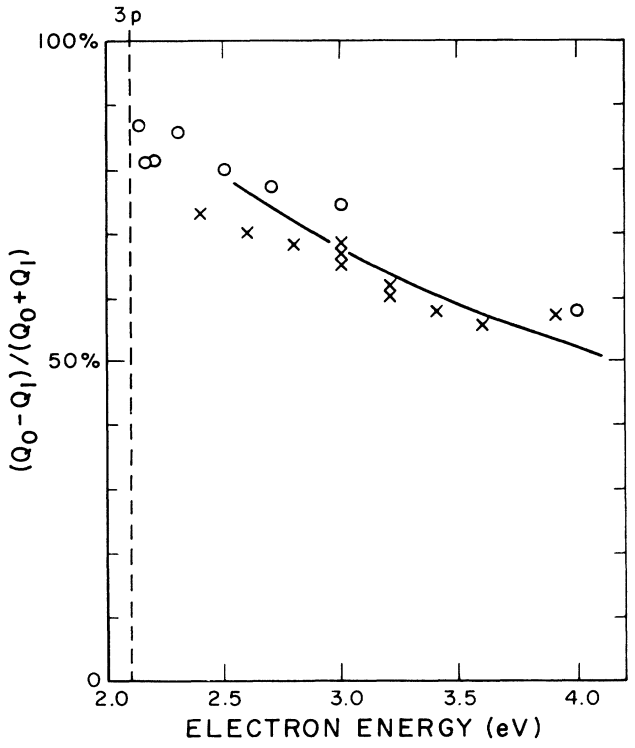

FIG. 11. Reduced polarization, $(Q_0-Q_1)/(Q_0+Q_1)$, including the present measurement (×), the measurement of Ref. 11 (——), and the calculation of Ref. 14 (○).

B. Differential, partial cross sections

The angularly differential character of the partial cross sections will now be discussed. The $Q_j^i(x)$ in Fig. 10 are the primary results of the experiment. As described above, these $Q_j^i(x)$ were obtained by least-squares fitting the constants in Eq. (3) using increasing $L_{\max}$ until convergence was obtained, and sometimes also averaging over small oscillations. We will compare these to theoretical $Q_j^i(\theta)$ from the Moores and Norcross calculation, which is the only publication with sufficient detail to allow evaluation of these differential cross sections. But before doing that it is of interest to see how well the truncated expansion in Eq. (3) can fit these theoretical $Q_j^i(x)$. If a good fit is obtained for the $L_{\max}$ used to analyze the data, then the limitations of this truncated expansion is probably not the cause of any discrepancies between theory and experiment. Two such comparisons are given in Fig. 12 where it is seen that excellent fits are obtained. On the other hand, the theoretical $Q_1^0(x)$ suddenly decreases to zero between $x=0.93$ and 1.0, whereas the Eq. (3) expansion with $l_{\max}=3$ is clearly not capable of representing such behavior. In this case only the area under the forward peak should be the same for the experimental and theoretical $Q(x)$.

The Moores and Norcross paper only provides R-matrix values at a few energies, of which the 3.0- and 4.0-eV values are closest to our 2.6-, 3.1-, and 3.6-eV data. To show E dependences we have replotted our data versus E in Fig. 13. Here one sees that overall the various $Q_j^i(x)$ vary systematically with E within the energy range probed. [However, the Q_0^1 at the right side of Fig. 13(c) are somewhat inconsistent, as these have a very

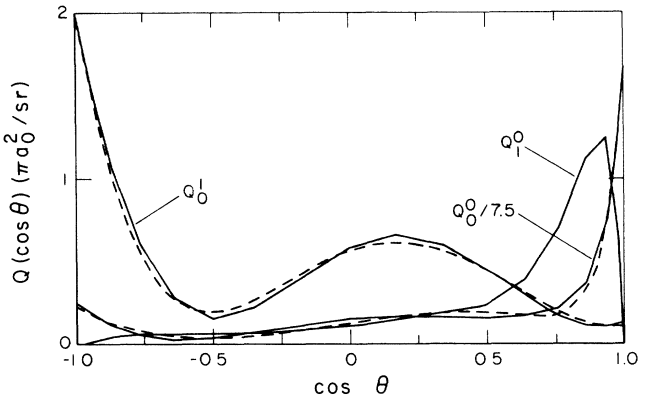

FIG. 12. Test of the ability of Eq.(3) to fit the theoretical $Q_j^i(x)$ from Ref. 14. The theoretical values are represented by a solid line connecting the values at calculated angles, which are at breaks in the curve; Eq. (3) fits are dashed line.

large uncertainty in this region where a much larger Q_1^0 also contributes to the measured $m_J = -\frac{1}{2}$ signal (see Fig. 10). Note, also, that $Q_1^0(x)$ does not vary systematically at the left side of Fig. 13(b). This fluctuation is an example of the small-Δx or high-frequency oscillations that are poorly established by the deconvolution.] In particular, the higher-angle ($x < 0.5$) portions of all the Q_j^i decrease slowly with increasing energy, and the forward peaks increase rapidly with increasing energy. Thus, it is quite easy to compare to the theoretical $Q_j^i(x)$ in spite of the minor energy differences, as is done in Fig. 13. Note that the calculation and experiment are in reasonable agreement regarding the overall shape and forward or backward peaking. On the other hand, there are significant differences when detailed shapes are considered. Some of these differences are larger than the experimental uncertainties, but fractionally small Q regions and relatively rapid undulation differences should be disregarded.

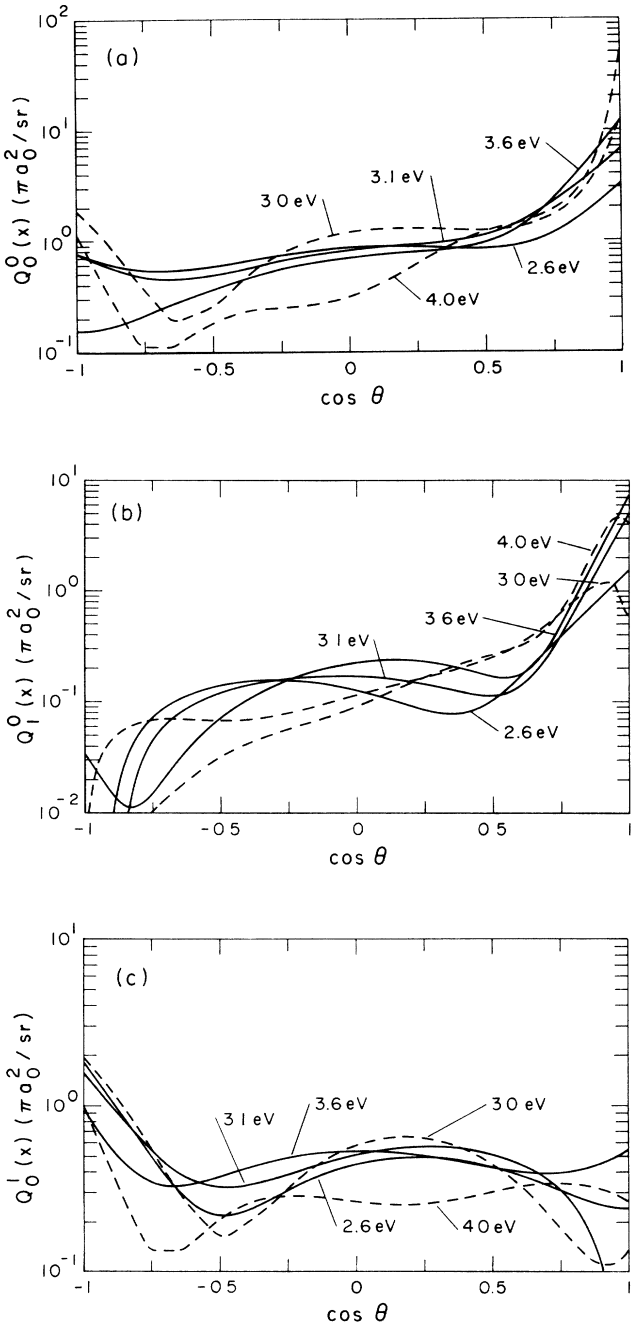

FIG. 13. Comparison of the measured $Q_j^i(x)$ (solid lines) to the Moores and Norcross calculation (dashed lines). Note that the experimental energies are 2.6, 3.1, and 3.6 eV, whereas the calculation is at 3.0 and 4.0 eV; (a) is $Q_0^0(x)$, (b) is $Q_1^0(x)$, and (c) is $Q_0^1(x)$.

The presence or absence of forward peaking in these Q_j^i has a simple "physical" explanation, in that $\Delta m_s = 0$ excitation is optically allowed and therefore expected for large impact parameter collisions that produce small deflections. Similarly, $\Delta m_L = 0$ is most "allowed" and long-range near threshold, again emphasizing forward scattering. For Q_0^0 both Δm_s and Δm_l are thus "allowed" and strong forward peaking is expected and found. In contrast Q_0^1 involves spin exchange and is the least likely at long range; and it is indeed observed to have a backward peak. Another well-known and understood phenomena is the shift of each $Q_j^i(\theta)$ toward forward angles as the collision energy is increased. However, the relatively constant Q_j^i shape at higher angles for $E_f = 0.5-1.5$ eV was not expected.

VII. CONCLUSIONS

The energy and angular dependence of the three differential cross sections in Fig. 13 offers a unique overview of near-threshold electron excitation; here the energy range is from 1.24 to 1.71 times the threshold energy. The partial cross section Q_0^1 which results from spin exchange is backward peaked, and as collision energy increases this backward peak decreases while the forward-angle parts increase slowly. The total Q_0^1 thus changes little across this energy range. The two $\Delta m_s = 0$ partial cross sections (Q_0^0 and Q_1^0) are forward peaked, and the forward peak increases with increasing energy while the high-angle portions decrease. (Look at the overall trends at higher angles to see this, recognizing that this region represents a small portion of the total Q_i^0 and thus is fractionally less accurate.) The forward-peaked character of these two Q_i^0 is consistent with expectations for the very-long-range character of this dipole-allowed cross section, whose overall size is ~ 30 Å^2. It can be seen that $Q_0^0/Q_1^0 \gg 1$ and it increases near threshold, as expected from the Percival and Seaton threshold condition $Q_0^0/Q_1^0 = \infty$. Also, it is interesting that this Q_0^0/Q_1^0 ratio generally increases with angle, as expected from the Born approximation relationship between Δm_l and Δk direction. The presence of undulations in Q_0^1 and Q_1^0 is interesting, but we do not have any simple explanations or know if this is a general characteristic. Most or all of these trends and characteristics are probably a general property of near threshold excitation of dipole-allowed transitions.

The partial cross sections calculated by Moores and Norcross (MN) are typically within 20% agreement with the measurements for the three largest Q_j^i components (Fig. 4). For electron energies below the 4S threshold

there is no cascading from higher-lying electron-excited states, and the data may be compared directly to their calculated values. Here the measured Q_0^0 values are generally about 10% smaller than those of MN, while the Q_1^0 data are ~20% larger, excepting the anomalous 2.28-eV value. Overall, these results serve to emphasize the important role that spin exchange plays in the low-energy excitation process.

As noted in our previous publication, there appears to be a discrepancy between the measured Q_1^1 results and the calculated values of MN below the 4S threshold. Cross-section mixing effects due to spiraling appear insufficient to account for the observed difference, as these primarily add a fraction of $Q_0^{|\Delta m_s|}$ to each $Q_1^{|\Delta m_s|}$. For example, even if the entire discrepancy between our measured reduced polarization and the average of that measured by Enemark and Gallagher (Fig. 9) were attributable to spiraling, this would yield an apparent enhancement of less than 20% in the Q_1^1 cross section at 2.8 eV.

We conclude that this calculation, which has stood the test of time amazingly well, could now be significantly improved in the light of current experimental advances. We hope that such an effort would provide valuable and far-reaching insights into near-threshold electron excitation of atoms.

As already noted, this experiment provides four partial cross sections for Na $3S \rightarrow 3P$ excitation but not their three relative phases. During the course of our work, Kelly, McClelland, and Celotta have succeeded in measuring several other partial components of this excitation cross section,[4] using spin-polarized electron beams. Since neither experiment yet detects the full set of seven cross section parameters, and their quantization axes are rotated by 90°, it is not possible to directly intercompare experimental results. Although this was unplanned, the two experiments complement each other. Since the ultimate goal is to test physical understanding of the electron-excitation process, each experiment provides an independent comparison to the predictions of the best available theories.

ACKNOWLEDGMENTS

This work was supported by the Fundamental Interactions Branch of the Division of Chemical Sciences, Office of Basic Energy Sciences, Office of Energy Research, Department of Energy. We wish to thank K. Gibble for developing the digital laser-frequency controller, and M. Troyer for assistance with the analysis of the angular distributions.

APPENDIX: POWER-DEPENDENCE CORRECTION

Since the linearly polarized ν_2 laser propagates along the magnetic-field direction, it excites the four $\Delta m_J = \pm 1$, $3P_{3/2}$-$5S_{1/2}$ Zeeman transitions shown in Fig. 1. ($3P_{3/2}$ and $5S_{1/2}$ will be discussed as fully hyperfine decoupled in the 218-G magnetic field; corrections of a few percent size are actually made in the data analysis.) The transition strength for the two transitions originating from $|m_J| = \frac{3}{2}$ is a factor of three larger than from $|m_J| = \frac{1}{2}$, so at low ν_2-laser power or far-off resonance the probability that an atom electron excited to $|m_J| = \frac{3}{2}$ emits a 4P-state fluorescence photon is three times that of an atom excited to $|m_J| = \frac{1}{2}$. This ratio becomes approximately unity as the $3P_{3/2}(m_J)$-$5S(m_s'')$ transition is saturated in the high-power limit for ν_2 on resonance. In Ref. 6 we show the rate equations used to calculate the resulting power-dependent proportionality between the areas under each $|m_J|$ component. These include laser-radiation coupling of one $3P_{3/2}(m_J)$ to $5S(m_s'')$ transition plus spontaneous-emission between $5S(m_s'')$, 4P, $3P_J(m_J)$, and 3S levels. Also, we average over the Gaussian laser-beam intensity profile. The resulting calculated power dependence of these $|m_J| = \frac{1}{2}$ versus $\frac{3}{2}$, 4P-fluorescence detection efficiencies is given in Ref. 6, where it has been shown to fit the observations. Overall, Q_j^i are uncertain by ~2% due to power-dependence uncertainty. Most of the angle-integrated cross section data scans were taken at a power density of ~0.8 W/cm^2, while the differential cross sections were measured using ~10% of this power.

*Present address: Department of Physics, University of Idaho, Moscow, ID 83843.

†Present address: Department of Physics, University of Virginia, Charlottesville, VA 22903.

‡Quantum Physics Division, National Institute of Standards and Technology.

[1] J. Kessler, *Polarized Electrons*, 2nd ed. (Springer-Verlag, Berlin, 1985).

[2] B. Bederson, Comments At. Mol. Phys. **1**, 41 (1969); **1**, 65 (1969).

[3] P. J. O. Teubner, J. L. Riley, M. J. Brunger, and S. J. Buckman, J. Phys. B **19**, 3313 (1986) (see references within).

[4] J. J. McClelland, M. H. Kelley, and R. J. Celotta, Phys. Rev. Lett. **56**, 1362 (1986); Phys. Rev. A **40**, 2321 (1989).

[5] X. L. Han, G. W. Schinn, and A. Gallagher, Phys. Rev. A **38**, 535 (1988).

[6] X. L. Han, Ph.D. dissertation, University of Colorado, Boulder, 1989.

[7] G. W. Schinn, Ph.D. dissertation, University of Colorado, Boulder, 1988.

[8] J. F. Kelly and A. Gallagher, Rev. Sci. Instrum. **58**, 563 (1987).

[9] G. W. Schinn, X. L. Han, and A. Gallagher, J. Opt. Soc. Am. B (to be published).

[10] B. Stumpf and A. C. Gallagher, Phys. Rev. A **32**, 3344 (1985).

[11] E. A. Enemark and A. C. Gallagher, Phys. Rev. A **6**, 192 (1972).

[12] P. O. Taylor, K. T. Dolder, W. E. Kauppila, and G. H. Dunn, Rev. Sci. Instrum. **45**, 538 (1974).

[13] M. J. Coulombe and A. S. Pine, Appl. Opt. **18**, 1505 (1979).

[14] D. L. Moores and D. W. Norcross, J. Phys. B **5**, 1482 (1972).

[15] J. Mitroy (private communication).

[16] J. O. Phelps and C. C. Lin, Phys. Rev. A **24**, 1299 (1981).

[17] S. T. Chen and A. C. Gallagher, Phys. Rev. **17**, 551 (1978).

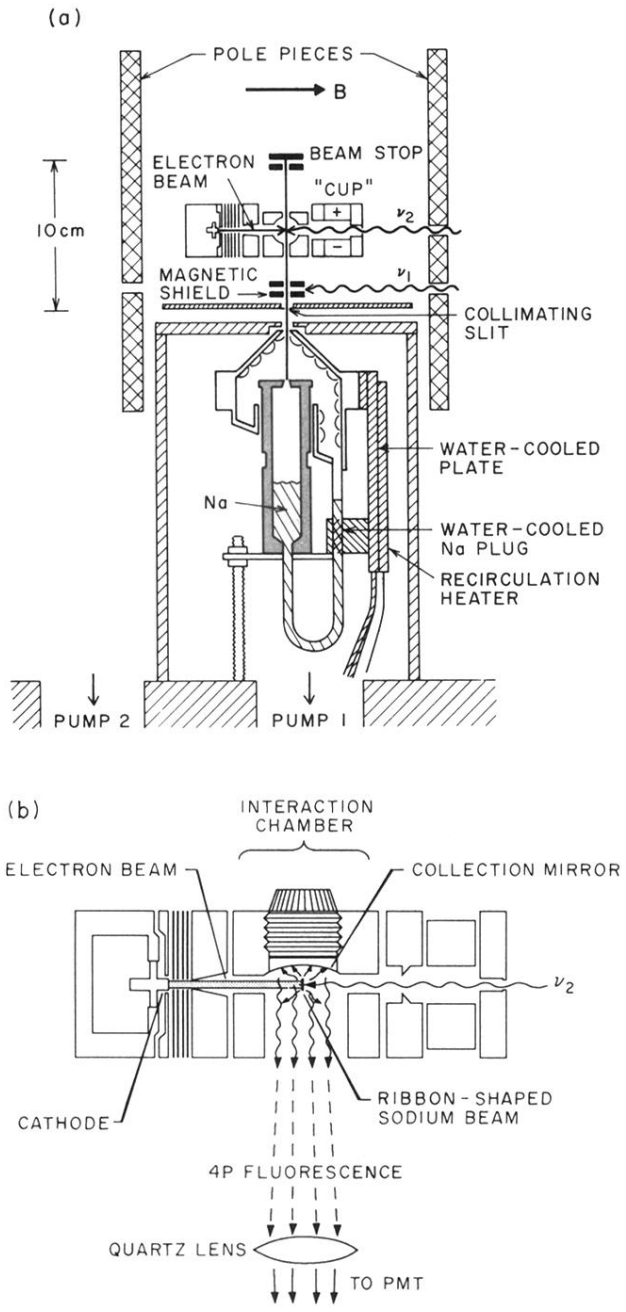

FIG. 3. Cross section of the apparatus (a) in the plane of the Na and electron beams and (b) in the plane of the detection optics and electron beams. The latter includes details of the electron gun. A fine Cu screen shielded the interaction region from possible charging of the insulating mirror surface.